model theory is presented in detail, and the predictions from the model are compared to experimental data for a radiation crosslinked UHMWPE material.

2. Experimental Data

To guide the material model development we used existing experimental data for a crosslinked UHMWPE that was gamma radiation crosslinked at a dose of 100 kGy. The full details of the UHMWPE material and the experimental testing can be found elsewhere (Bergström *et al.*, 2002); however, a brief summary of the experimental procedure and data are summarized here. The specimens were machined from ram-extruded GUR 1050 (Kurtz *et al.*, 2002), and then heat treated at 110°C for 2 hours. The test specimens had a degree of crystallinity of 61%.

The material was tested in uniaxial tension, uniaxial compression, uniaxial cyclic loading, and in biaxial punch loading. The uniaxial tension tests were performed on dogbone-shaped specimens with a diameter of 10 mm in the gauge section and a gauge length of 25 mm. The tension specimens were deformed in displacement control using different applied engineering strain rates to final failure. All tests were performed at room temperature. A non-contact video extensometer was used to measure the uniaxial strain by tracking the displacement of two surface marks in the gauge section of the specimen. The uniaxial compression experiments were performed on test specimens with a diameter of 10 mm and a height of 15 mm. The specimens were uniaxially compressed at constant engineering strain rate. The experiments were performed at room temperature. A compressometer spanning the parallel test platens was used to measure the axial strain. The test platens were polished and lubricated with liquid soap to minimize frictional end effects. No barreling of the test specimens was observed in the compression experiments. In all uniaxial experiments, the true stress and true strain histories were calculated from the raw force-displacement data assuming a homogeneous constant volume deformation. The results from the uniaxial testing are summarized in Figures 1a and 1b. These figures show that UHMWPE is almost linear elastic for strains less than 0.01, and then starts to undergo distributed yielding until the onset of large-scale yielding at a true strain of 0.05. As the applied strain continues to increase the material gradually stiffens due to the entropic resistance created by the deformation induced molecular orientation. The true stress response is almost symmetrical between tension and compression for true strains up to 0.5. The figures also show that the material is relatively weakly strain-rate dependent.

In addition to the uniaxial experimental tests, a third set of experiments were performed on penny-shaped specimens with a diameter of 6.4 mm, and thickness of 0.5 mm. In these tests the specimens were loaded in displacement control using a hemispherical punch head with a diameter of 0.254 mm moving at a constant rate of 0.5 mm/min. The punch experiments were performed at room temperature according to ASTM F2183 (2002). Figure 2a shows a FE representation of the experimental setup, and Figure 2b shows the measured force-displacement response. This figure shows that the force-displacement behavior is almost linear up to a punch displacement of about 1.7 mm. The non-linearity in the force-displacement data that is introduced at this point is created by biaxial necking that causes the specimen to become thinner in a circumferential region. As the deformation increases the material strain hardens until final failure occurs at about 2.4 mm punch displacement.

All uniaxial and small punch tests were performed on 5 different specimens. The variability in the stress (force) between the repeated tests was less than 5%, and the experimental results that are presented here are the median stress-strain curve for each condition.

3. Constitutive Model

The material response summarized in the previous section can be captured using a three network representation. The three-network model consists of three parts, or molecular networks, acting in parallel, see the rheological representation in Figure 3b. In this model the initial viscoplastic response is captured using two separate energy activation mechanisms corresponding to amorphous and semicrystalline domains, and the large strain response is controlled by entropic resistance, see Figure 3a.

In this model framework the deformation gradient acting on network A is multiplicatively decomposed into elastic and viscoplastic components: $\mathbf{F} = \mathbf{F}^e_A \mathbf{F}^v_A$. The Cauchy stress acting on network A is given by a temperature-dependent version of the eight-chain model (Arruda and Boyce, 1993; Bergström and Boyce, 2000):

$$\boldsymbol{\sigma}_A = \frac{\mu_A}{J^e_A \overline{\lambda^{e*}_A}} \left[1 + \frac{\theta - \theta_0}{\hat{\theta}} \right] \frac{\mathcal{L}^{-1}\left(\overline{\lambda^{e*}_A}/\lambda_L\right)}{\mathcal{L}^{-1}(1/\lambda_L)} \operatorname{dev}\left[\mathbf{b}^{e*}_A\right] + \kappa(J^e_A - 1)\mathbf{1}, \tag{1}$$

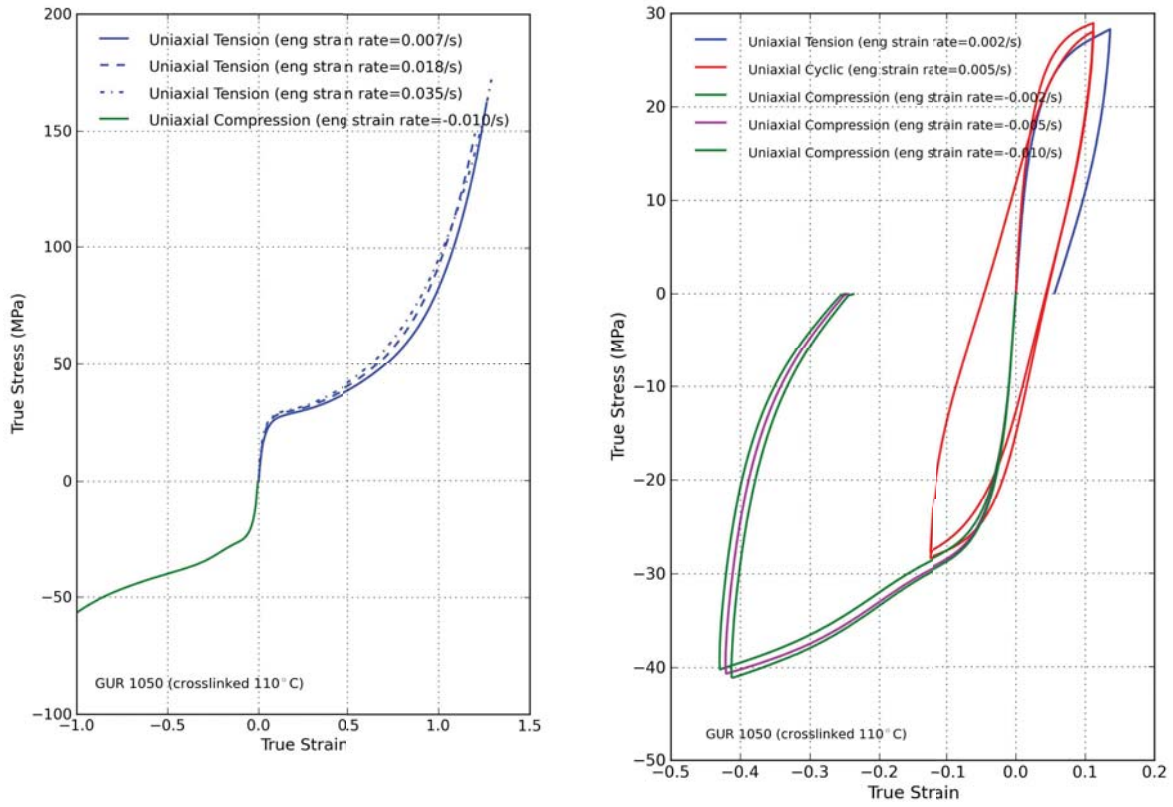

(a) (b)

Figure 1: Experimental data for UHMWPE in uniaxial tension, compression, and cyclic loading. All experiments were performed at room temperature.

where $J_A^e = \det[\mathbf{F}_A^e]$, μ_A is the initial shear modulus, λ_L is the chain locking stretch, θ is the current temperature, θ_0 is a reference temperature, $\hat{\theta}$ is a material parameter specifying the temperature response of the stiffness, $\mathbf{b}_A^{e*} = (J_A^e)^{-2/3}\mathbf{F}_A^e(\mathbf{F}_A^e)^\top$ is the Cauchy-Green deformation tensor, $\overline{\lambda_A^{e*}} = \left(\mathrm{tr}[\mathbf{b}_A^{e*}]/3\right)^{1/2}$ is the effective chain stretch based on the eight-chain topology assumption (Arruda and Boyce, 1993), $\mathcal{L}^{-1}(x)$ is the inverse Langevin function, where $\mathcal{L}(x) = \coth(x) - 1/x$, and κ is the bulk modulus. The temperature dependence can be further tailored by using normalized modulus data for different temperatures obtained from, for example, dynamic mechanical analysis (DMA).

The viscoelastic deformation gradient acting on network B is also decomposed into elastic and viscoplastic parts: $\mathbf{F} = \mathbf{F}_B^e\mathbf{F}_B^v$. The Cauchy stress acting on network B is obtained from the same eight-chain network representation that was used for network A:

$$\boldsymbol{\sigma}_B = \frac{\mu_B}{J_B^e\overline{\lambda_B^{e*}}}\left[1 + \frac{\theta - \theta_0}{\hat{\theta}}\right]\frac{\mathcal{L}^{-1}\left(\overline{\lambda_B^{e*}}/\lambda_L\right)}{\mathcal{L}^{-1}(1/\lambda_L)}\,\mathrm{dev}\,[\mathbf{b}_B^{e*}] + \kappa(J_B^e - 1)\mathbf{1}, \tag{2}$$

where $J_B^e = \det[\mathbf{F}_B^e]$, μ_B is the initial shear modulus, $\mathbf{b}_B^{e*} = (J_B^e)^{-2/3}\mathbf{F}_B^e(\mathbf{F}_B^e)^\top$ is the Cauchy-Green deformation tensor, and $\overline{\lambda_B^{e*}} = \left(\mathrm{tr}[\mathbf{b}_B^{e*}]/3\right)^{1/2}$. In Equation (2), the effective shear modulus is taken to evolve with plastic strain from an initial value of μ_{Bi} to a final value of μ_{Bf} according to:

$$\dot{\mu}_B = -\beta\left[\mu_B - \mu_{Bf}\right]\cdot\dot{\gamma}_A, \tag{3}$$

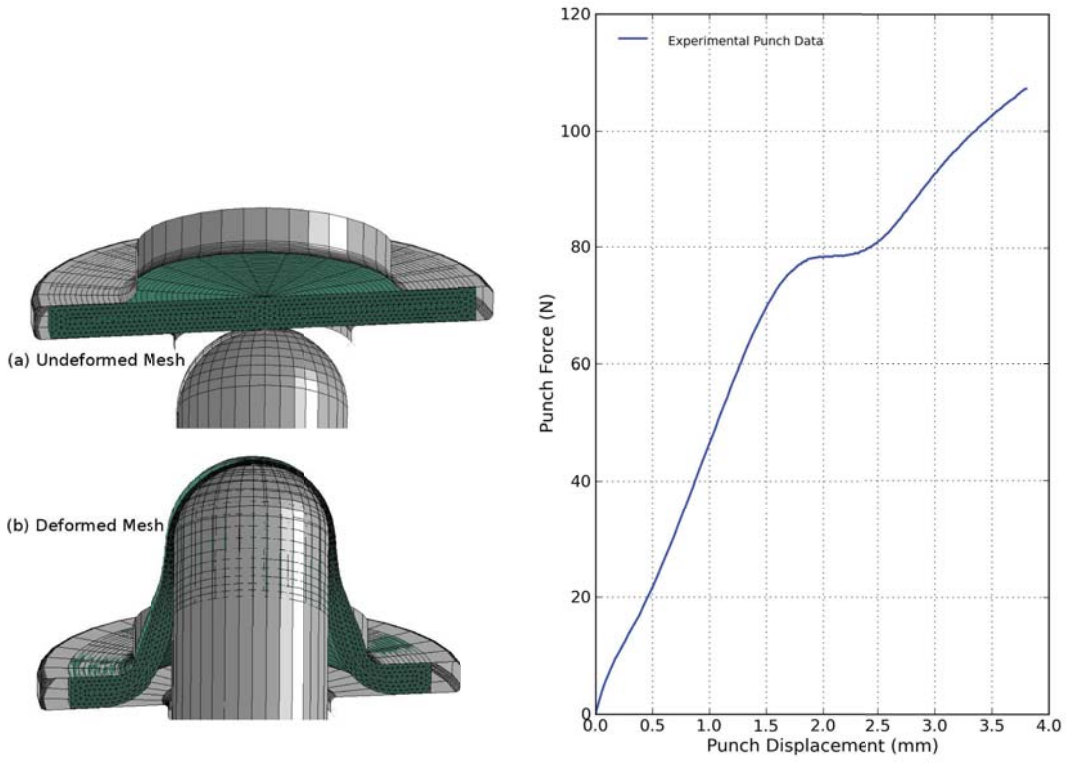

(a) (b)

Figure 2: (a) Finite element representation of the experimental punch test. The simulation was performed using Abaqus/Standard with 550 CAX6MH elements. (b) Experimental data for UHMWPE in small punch loading. The experiment was performed at room temperature.

where $\dot{\gamma}_A$ is the viscoplastic flow rate to be defined in Equation (5). By evolving the stiffness with plastic strain the model is able to capture the evolution from initial yielding to large scale flow.

The Cauchy stress acting on network C is given by the eight-chain model with first order I_2 dependence[1]:

$$\boldsymbol{\sigma}_C = \frac{1}{1+q}\left\{\frac{\mu_C}{J\lambda_{chain}}\left[1+\frac{\theta-\theta_0}{\hat{\theta}}\right]\frac{\mathcal{L}^{-1}\left(\frac{\lambda_{chain}}{\lambda_L}\right)}{\mathcal{L}^{-1}\left(\frac{1}{\lambda_L}\right)}\,\mathrm{dev}\left[\mathbf{b}^*\right]+\kappa(J-1)\mathbf{1}+q\frac{\mu_c}{J}\left[I_1^*\mathbf{b}^*-\frac{2I_2^*}{3}\mathbf{I}-(\mathbf{b}^*)^2\right]\right\}, \tag{4}$$

where $J = \det[\mathbf{F}]$, μ_C is the initial shear modulus, $\mathbf{b}^* = J^{-2/3}\mathbf{F}(\mathbf{F})^\top$ is the Cauchy-Green deformation tensor, $\lambda_{chain} = (\mathrm{tr}[\mathbf{b}^*]/3)^{1/2}$, and q controls the magnitude of the I_2-dependence.

In summary, using this framework the total Cauchy stress in the system is given by the sum of the stresses in each network: $\boldsymbol{\sigma} = \boldsymbol{\sigma}_A + \boldsymbol{\sigma}_B + \boldsymbol{\sigma}_C$.

To complete the description of the material model framework it is necessary to also specify the rate kinematics. Here, the total velocity gradient of network A, $\mathbf{L} = \dot{\mathbf{F}}\mathbf{F}^{-1}$, can be decomposed into elastic and viscous components: $\mathbf{L} = \mathbf{L}_A^e + \mathbf{F}_A^e\mathbf{L}_A^v\mathbf{F}_A^{e-1} = \mathbf{L}_A^e + \tilde{\mathbf{L}}_A^v$, where $\mathbf{L}_A^v = \dot{\mathbf{F}}_A^v\mathbf{F}_A^{v-1} = \mathbf{D}_A^v + \mathbf{W}_A^v$ and $\tilde{\mathbf{L}}_A^v = \tilde{\mathbf{D}}_A^v + \tilde{\mathbf{W}}_A^v$. The unloading process relating the deformed state with the intermediate state is not uniquely defined since an arbitrary rigid body rotation of the intermediate state

[1]This representation is similar to the Mooney-Rivlin model with non-Gaussian chain statistics.

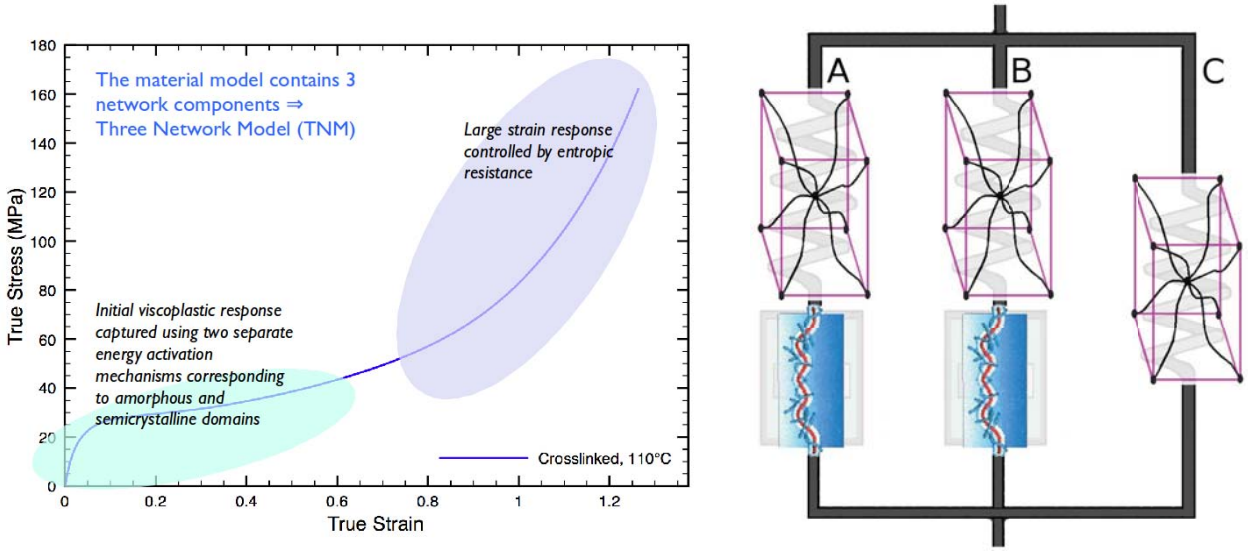

(a) (b)

Figure 3: (a) The stress-strain curve is separated into different domains each controlled by different deformation mechanisms. (b) Rheological representation of the constitutive model.

still leaves the state stress free. The intermediate state can be made unique in different ways (Boyce *et al.*, 1989), one particularly convenient way that is used here is to prescribe $\tilde{\mathbf{W}}_A^v = \mathbf{0}$. This will, in general, result in elastic and inelastic deformation gradients both containing rotations. The rate of viscoplastic flow of network A is then constitutively prescribed by $\tilde{\mathbf{D}}_A^v = \dot{\gamma}_A \mathbf{N}_A$. The tensor $\mathbf{N}_A$ specifies the direction of the driving deviatoric stress of the relaxed configuration convected to the current configuration, and the term $\dot{\gamma}_A$ specifies the effective deviatoric flow rate. Noting that $\boldsymbol{\sigma}_A$ is computed in the loaded configuration, the driving deviatoric stress on the relaxed configuration convected to the current configuration is given by $\boldsymbol{\sigma}'_A = \mathrm{dev}[\boldsymbol{\sigma}_A]$, and by defining an effective stress by the Frobenius norm $\tau_A = \|\boldsymbol{\sigma}'_A\|_F \equiv \left(\mathrm{tr}[\boldsymbol{\sigma}'_A \boldsymbol{\sigma}'_A]\right)^{1/2}$, the direction of the driving deviatoric stress becomes $\mathbf{N}_A = \boldsymbol{\sigma}'_A / \tau_A$. The effective deviatoric flow rate is given by the power-flow equation:

$$\dot{\gamma}_A = \dot{\gamma}_0 \cdot \left(\frac{\tau_A}{\hat{\tau}_A + aR(p_A)} \right)^{m_A} \cdot \left(\frac{\theta}{\theta_0} \right)^n , \tag{5}$$

where $\dot{\gamma}_0 \equiv 1/\mathrm{s}$ is a constant introduced for dimensional consistency, $p_A = -[(\boldsymbol{\sigma}_A)_{11} + (\boldsymbol{\sigma}_A)_{22} + (\boldsymbol{\sigma}_A)_{33}]/3$ is the hydrostatic pressure, $R(x) = (x + |x|)/2$ is the ramp function, and $\hat{\tau}_A$, a, m_A, and n are specified material parameters. In this framework, the temperature dependence of the flow rate is taken to follow a power law form. In summary, the velocity gradient of the viscoelastic flow of network A can be written

$$\dot{\mathbf{F}}_A^v = \dot{\gamma}_A \mathbf{F}_A^{e-1} \frac{\mathrm{dev}[\boldsymbol{\sigma}_A]}{\tau_A} \mathbf{F}. \tag{6}$$

The total velocity gradient of network B can be obtained similarly to network A. Specifically, $\mathbf{L} = \dot{\mathbf{F}}\mathbf{F}^{-1}$ can be decomposed into elastic and viscous components: $\mathbf{L} = \mathbf{L}_B^e + \mathbf{F}_B^e \mathbf{L}_B^v \mathbf{F}_B^{e-1} = \mathbf{L}_B^e + \tilde{\mathbf{L}}_B^v$, where $\mathbf{L}_B^v = \dot{\mathbf{F}}_B^v \mathbf{F}_B^{v-1} = \mathbf{D}_B^v + \mathbf{W}_B^v$ and $\tilde{\mathbf{L}}_B^v = \tilde{\mathbf{D}}_B^v + \tilde{\mathbf{W}}_B^v$. As for Network A, the intermediate state is specified by taking $\tilde{\mathbf{W}}_B^v = \mathbf{0}$. The rate of viscoplastic flow of network B is constitutively prescribed by $\tilde{\mathbf{D}}_B^v = \dot{\gamma}_B \mathbf{N}_B = \mathrm{dev}[\boldsymbol{\sigma}_B]/\tau_B$, where $\tau_B = \|\boldsymbol{\sigma}'_B\|_F \equiv \left(\mathrm{tr}[\boldsymbol{\sigma}'_B \boldsymbol{\sigma}'_B]\right)^{1/2}$. The effective deviatoric flow rate is given by the power-flow equation:

$$\dot{\gamma}_B = \dot{\gamma}_0 \cdot \left(\frac{\tau_B}{\hat{\tau}_B + aR(p_B)} \right)^{m_B} \cdot \left(\frac{\theta}{\theta_0} \right)^n , \tag{7}$$

Table 1: Material parameters used by the three-network model. The material parameters controlling the temperature dependence have been omitted since all experiments were performed at room temperature.

Symbol	Value	Description
μ_A	200 MPa	Shear modulus of network A
λ_L	3.25	Locking stretch
κ	6000 MPa	Bulk modulus
$\hat{\tau}_A$	3.25 MPa	Flow resistance of network A
a	0.073	Pressure dependence of flow
$m_A = m_b$	20	Stress exponential of network A
μ_{Bi}	293 MPa	Initial shear modulus of network B
μ_{Bf}	79.1 MPa	Final shear modulus of network B
β	31.9	Evolution rate of μ_B
$\hat{\tau}_B$	20.1 MPa	Flow resistance of network B
μ_C	10.0 MPa	Shear modulus of network C
q	0.23	Relative contribution of I_2 of network C

where $\dot{\gamma}_0 \equiv 1/\text{s}$ is a constant introduced for dimensional consistency, $p_B = -[(\boldsymbol{\sigma}_B)_{11} + (\boldsymbol{\sigma}_B)_{22} + (\boldsymbol{\sigma}_B)_{33}]/3$ is the hydrostatic pressure, and $\hat{\tau}_B$, a, m_B, and n are specified material parameters. In this framework, the temperature dependence of the flow rate is taken to follow a power law form. In summary, the velocity gradient of the viscoelastic flow of network B can be written:

$$\dot{\mathbf{F}}_B^v = \dot{\gamma}_B \mathbf{F}_B^{e-1} \frac{\text{dev}[\boldsymbol{\sigma}_B]}{\tau_B} \mathbf{F}. \tag{8}$$

The required material parameters for the material model are listed in Table 1.

4. Results

The new three network material model was calibrated to the uniaxial experimental data using a two step procedure. First three key material parameters were estimated using the following graphical approach:

1. μ_c was obtained from one third of the uniaxial tangent modulus[2] at an intermediate strain of $\varepsilon_{true} = 0.5$.
2. μ_{Bf} was estimated from 1/3 of the initial Young's modulus.
3. $\hat{\tau}_B$ was estimated from 1/3 of the final yield stress.

The remaining material parameters were estimated using the following approximate relations: $\mu_A = \mu_{Bi}/2 = \mu_C$, $\lambda_L = 3$, $\kappa = 6000$ MPa, $\hat{\tau}_A = \hat{\tau}_B/5$, $a = 0.05$, $m_A = m_B = 20$, $\beta = 30$, and $q = 0.2$. After the initial guesses of the material parameters were established, the parameter set was optimized using a minimization algorithm based on the Nelder-Mead simplex method. This optimization of the parameters was based on the complete set of uniaxial data. The resulting material parameters are listed in Table 1.

A direct comparison between the experimental data and the model predictions is shown in Figures 4a and 4b. These figures demonstrate that the calibrated material model captures the yield evolution, the difference in flow behavior in tension and compression, the strain-rate dependence, and the cyclic loading response.

To validate the material model it was implemented into an Abaqus user material subroutine (UMAT and VUMAT) and then used in an axisymmetric finite element model of the small punch experiment. In this simulation the contact between the UHMWPE specimen and the fixture and punch was taken to have a friction coefficient of 0.05. The results from the small punch simulation are shown in Figure 5. This figure illustrate that the calibrated material model accurately predicts the large-strain non-linear response of the small punch test.

[2]The 1/3 factor is used since the experimental data is uniaxial and μ_c is a shear modulus.

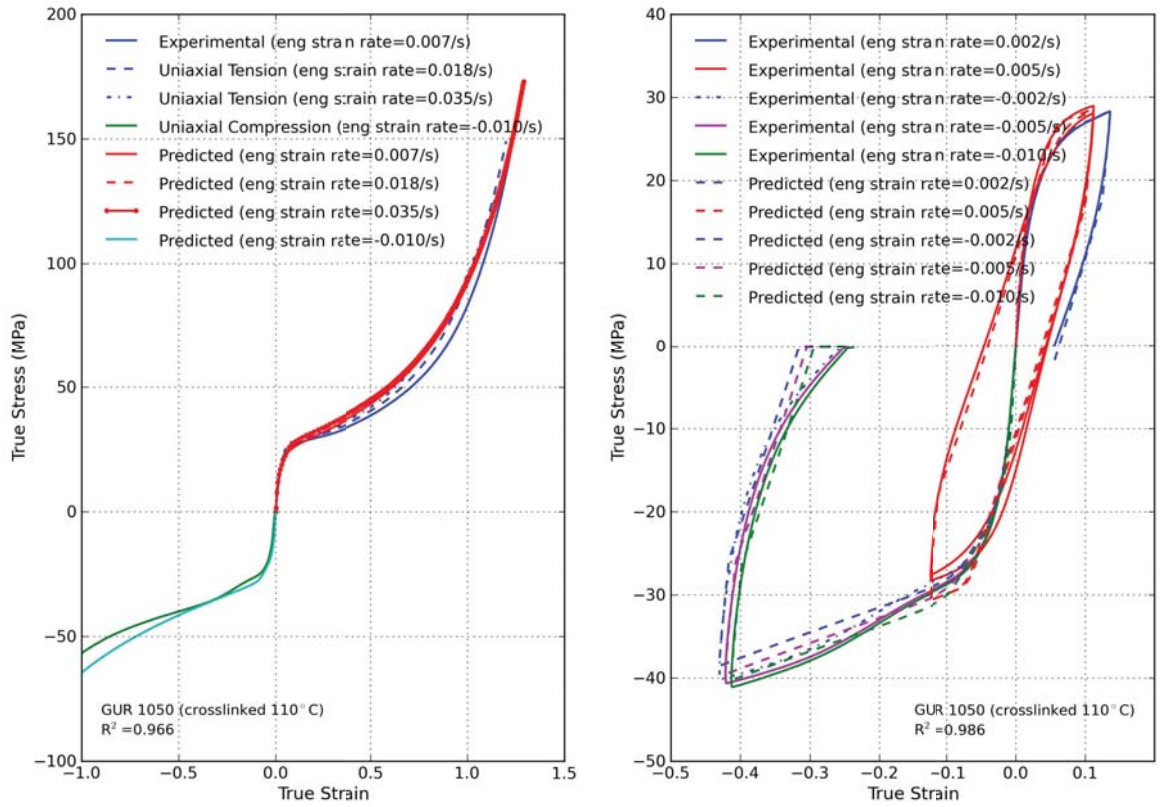

(a) (b)

Figure 4: Comparison between experimental data and model predictions for UHMWPE in uniaxial tension, compression, and cyclic loading. All experiments were performed at room temperature.

The coefficient of determination (R^2) of the new material model is summarized in Table 2 together with the predicted values of a selection of other material models. The table illustrates that the new three-network model is superior to the other models at predicting the complete set of experimental data.

Table 2: Summary of R^2 values for different material models.

Model	**R^2 for Uniaxial**	**R^2 for Small Punch**	**R^2 for Uniaxial and Punch**
New Three Network Model	0.977	0.994	0.986
Hybrid Model (Bergström *et al.*, 2004)	0.943	0.870	0.907
Bergström and Boyce (1998) Model	0.859	0.569	0.714
Plasticity model with kinematic hardening	0.684	0.141	0.413
Plasticity model with isotropic hardening	0.505	0.692	0.599

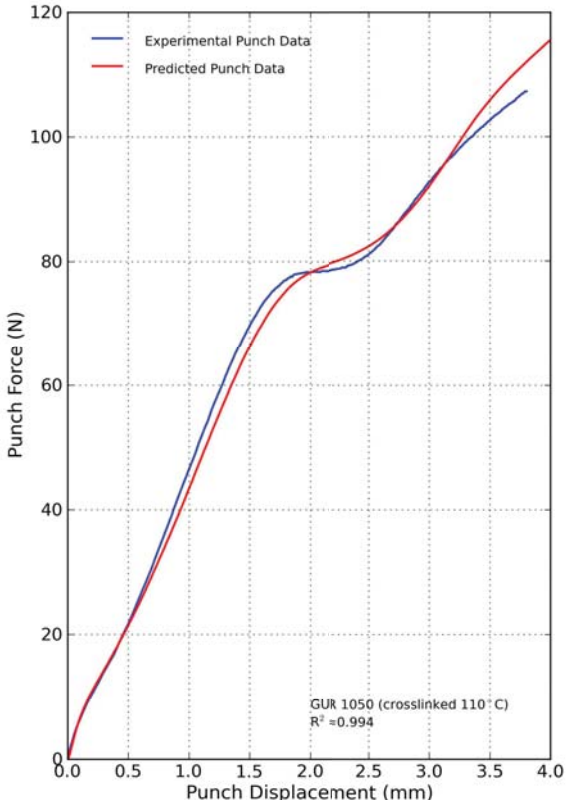

Figure 5: Comparison between experimental data and model predictions for UHMWPE in small punch loading. The experiment was performed at room temperature.

References

Arruda, E. and Boyce, M. (1995). Effects of strain rate, temperature and thermomechanical coupling on the finite strain deformation of glassy polymers, *Mech. Mater.* **19**, pp. 193–212.

Arruda, E. M. and Boyce, M. C. (1993). A three-dimensional constitutive model for the large stretch behavior of rubber elastic materials, *J. Mech. Phys. Solids.* **41**, 2, pp. 389–412.

Bergström, J., Kurtz, S., Rimnac, C. and Edidin, A. (2002). Constitutive modeling of ultra-high molecular weight polyethylene under large-deformation and cyclic loading conditions, *Biomaterials* **23**, pp. 2329–2343.

Bergström, J., Rimnac, C. and Kurtz, S. (2003). Prediction of multiaxial mechanical behavior for conventional and highly crosslinked UHMWPE using a hybrid constitutive model, *Biomaterials* **24**, pp. 1365–1380.

Bergström, J., Rimnac, C. and Kurtz, S. (2004). An augmented hybrid constitutive model for simulation of unloading and cyclic loading behavior of conventional and highly crosslinked uhmwpe, *Biomaterials* **25**, pp. 2171–2178.

Bergström, J. S. and Boyce, M. C. (1998). Constitutive modeling of the large strain time-dependent behavior of elastomers, *J. Mech. Phys. Solids* **46**, pp. 931–954.

Bergström, J. S. and Boyce, M. C. (2000). Large strain time-dependent behavior of filled elastomers, *Mechanics of Materials* **32**, pp. 620–644.

Boyce, M. C., Weber, G. G. and Parks, D. M. (1989). On the kinematics of finite strain plasticity, *J. Mech. Phys. Solids* **37**, 5, pp. 647–665.

F2183, A. (2002). Standard test method for small punch testing of ultra-high molecular weight polyethylene used in surgical implants, .

Hasan, O. A. and Boyce, M. C. (1993). Energy storage during inelastic deformation of glassy polymers, *Polymer* **34**, 24, pp. 5085–5092.

Kurtz, S., Rimnac, C., Jewett, C., Goldberg, V. and Edidin, A. (2000). The relationship between the clinical performance and large deformation mechanical behavior of retrieved UHMWPE tibial inserts, *Biomaterials* **21**, p. 28391.

Kurtz, S., Villarraga, M., Herr, M., Bergstrom, J., Rimnac, C. and Edidin, A. (2002). Thermomechanical behavior of virgin and highly crosslinked ultra-high molecular weight polyethylene used in total joint replacements, *Biomaterials* **23**, pp. 3681–3697.

Muratoglu, O., Bragdon, C., OConnor, D., M, M. J. and Harris, W. (2001). A novel method of cross-linking ultra-high-molecular-weight polyethylene to improve wear, reduce oxidation, and retain mechanical properties. *J. Arthroplasty* **16**, p. 149160.

van Dommelen, J., Parks, D., Boyce, M., Brekelmans, W. and Baaijens, F. (2003). Micromechanical modeling of the elasto-viscoplastic behavior of semi-crystalline polymers, *J. Mech. Phys. Solids* **51**, pp. 519–541.